Cloud condensation nuclei prediction error from application of Köhler theory: Importance for the aerosol indirect effect

Rafaella-Eleni P. Sotiropoulou,[1] Athanasios Nenes,[2] Peter J. Adams,[3] and John H. Seinfeld[4]

Received 25 July 2006; revised 6 December 2006; accepted 27 February 2007; published 19 June 2007.

[1] In situ observations of aerosol and cloud condensation nuclei (CCN) and the GISS GCM Model II' with an online aerosol simulation and explicit aerosol-cloud interactions are used to quantify the uncertainty in radiative forcing and autoconversion rate from application of Köhler theory. Simulations suggest that application of Köhler theory introduces a 10–20% uncertainty in global average indirect forcing and 2–11% uncertainty in autoconversion. Regionally, the uncertainty in indirect forcing ranges between 10–20%, and 5–50% for autoconversion. These results are insensitive to the range of updraft velocity and water vapor uptake coefficient considered. This study suggests that Köhler theory (as implemented in climate models) is not a significant source of uncertainty for aerosol indirect forcing but can be substantial for assessments of aerosol effects on the hydrological cycle in climatically sensitive regions of the globe. This implies that improvements in the representation of GCM subgrid processes and aerosol size distribution will mostly benefit indirect forcing assessments. Predictions of autoconversion, by nature, will be subject to considerable uncertainty; its reduction may require explicit representation of size-resolved aerosol composition and mixing state.

Citation: Sotiropoulou, R.-E. P., A. Nenes, P. J. Adams, and J. H. Seinfeld (2007), Cloud condensation nuclei prediction error from application of Köhler theory: Importance for the aerosol indirect effect, *J. Geophys. Res.*, *112*, D12202, doi:10.1029/2006JD007834.

1. Introduction

[2] The *Intergovernmental Panel on Climate Change* [2001] identified indirect aerosol forcing as one of the largest source of uncertainty in anthropogenic climate forcing, and urged the accurate representation of physicochemical processes linking aerosols and clouds in global models. Physically based approaches [*Abdul-Razzak et al.*, 1998; *Cohard et al.*, 1998; *Abdul-Razzak and Ghan*, 2000; *Cohard et al.*, 2000; *Nenes and Seinfeld*, 2003; *Fountoukis and Nenes*, 2005] rely on theory first introduced by *Köhler* [1921], in which aerosol is assumed to be composed of a mixture of deliquescent electrolytes and insoluble material. Subsequent modifications to Köhler theory consider more complex aerosol-water interactions, such as the presence of slightly soluble compounds [e.g., *Shulman et al.*, 1996], surfactants [*Shulman et al.*, 1996; *Facchini et al.*, 1999], black carbon inclusions [*Conant et al.*, 2002], soluble gases [*Kulmala et al.*, 1993], and solute dissolution kinetics [*Asa-Awuku and Nenes*, 2007].

[3] Assessing the applicability of Köhler theory (and its extensions) is required for improving predictions of aerosol-cloud interactions. The ultimate test is CCN "closure," or comparing predictions of CCN concentrations (from application of Köhler theory to measurements of size distribution and chemical composition) with measurements obtained with a CCN counter. A multitude of CCN closure studies have been carried out with varying degrees of success, with prediction errors usually within 10–50% [e.g., *Medina et al.*, 2007, and references therein]. In situ cloud drop number concentration (CDNC) closure studies [e.g., *Conant et al.*, 2004; *Meskhidze et al.*, 2005; *Fountoukis et al.*, 2007] are also a good test of Köhler theory, although the degree of closure depends on the accuracy of other measured parameters, such as droplet concentration and cloud updraft velocity.

[4] Closure studies typically focus on CCN prediction error, but do not relate it to uncertainty in the aerosol indirect effect; the latter remains an outstanding issue for constraining anthropogenic climate forcing. *Sotiropoulou et al.* [2006] first addressed this problem; using ground-based CCN and aerosol measurements in combination with the *Fountoukis and Nenes* [2005] cloud droplet formation parameterization, CDNC uncertainty resulting from application of Köhler theory was found to be roughly half the CCN prediction uncertainty for a wide range of aerosol concentration, updraft velocity and droplet growth kinetics. This study extends the analysis of *Sotiropoulou et al.*

[1]School of Earth and Atmospheric Sciences, Georgia Institute of Technology, Atlanta, Georgia, USA.
[2]Schools of Earth and Atmospheric Sciences and Chemical and Biomolecular Engineering, Georgia Institute of Technology, Atlanta, Georgia, USA.
[3]Departments of Civil and Environmental Engineering and Engineering and Public Policy, Carnegie Mellon University, Pittsburgh, Pennsylvania, USA.
[4]Departments of Chemical Engineering and Environmental Science and Engineering, California Institute of Technology, Pasadena, California, USA.

0148-0227/07/2006JD007834

[2006], and uses a global model to assess the uncertainty in cloud droplet number, indirect radiative forcing (i.e., "first" aerosol indirect effect) and autoconversion associated with application of Köhler theory. Hereon, the term "CCN prediction error" expresses the error arising from application of Köhler theory. CCN uncertainty associated with errors in predicted aerosol size distribution and chemical composition are left for a future study.

2. Description of Global Model

[5] The 9-layer NASA Goddard Institute for Space Studies (GISS) general circulation model (GCM) Model II' [*Hansen et al.*, 1983; *Del Genio et al.*, 1996] with $4^\circ \times 5^\circ$ horizontal resolution and nine vertical layers (from surface to 10 mbar) is used. The model simulates the emissions, transport, chemical transformation and deposition of chemical tracers such as sulfate (SO_4^{2-}), ammonium (NH_4^+), dimethyl sulfide (DMS), methanesulfonic acid (MSA), sulfur dioxide (SO_2), ammonia (NH_3), and hydrogen peroxide (H_2O_2). The model time step for these processes is one hour. A quadratic upstream module for advection of heat and moisture and a fourth-order scheme for tracer advection are used [*Del Genio et al.*, 1996]. Sea surface temperatures are climatologically prescribed.

[6] Moist convection is implemented by a mass flux scheme that considers entraining and nonentraining plumes, compensating subsidence and downdrafts [*Del Genio and Yao*, 1993]. Liquid water associated with convective clouds either precipitates, evaporates or detrains into the large-scale cloud cover within the model time step. Liquid water is carried as a prognostic variable in the large-scale cloud scheme [*Del Genio et al.*, 1996], allowing large-scale clouds to persist for several time steps.

[7] The parameterization of cloud formation follows the approach of *Sundqvist et al.* [1989], in which the grid cloud fraction is proportional to the difference between the average grid box relative humidity and the relative humidity in the clear fraction of the grid [*Del Genio et al.*, 1996]. Autoconversion of cloud water to precipitation is parameterized as [*Del Genio et al.*, 1996],

$$(\dot{q}_l)_{AU} = C_0 q_l \left\{ 1 - \exp\left[-\left(\frac{q_c}{q_{crit}} \right)^4 \right] \right\} \quad (1)$$

where $(\dot{q}_l)_{AU}$ is the autoconversion rate (s^{-1}), q_{crit} is the critical cloud water content for the onset of rapid conversion (g m^{-3}), C_0 is the limiting autoconversion rate (s^{-1}), q_c is the in-cloud liquid water content (g m^{-3}) and q_l is the liquid water mixing ratio.

[8] The GISS radiative scheme [*Hansen et al.*, 1983] computes the absorption and scattering of radiation by gases and particles. The gaseous absorbers included in the GCM are H_2O, CO_2, O_3, O_2, and NO_2, utilizing twelve spectrally noncontiguous, vertically correlated-k distribution intervals. Cloud and aerosol radiative parameters (extinction cross section, single scattering albedo, and asymmetry parameter) are treated using radiative properties obtained from Mie calculations for the global aerosol climatology of *Toon and Pollack* [1976]. Six intervals for the spectral dependence of Mie parameters for clouds, aerosol and Rayleigh scattering are used [*Hansen et al.*, 1983]. Multiple scattering of solar radiation utilizes the doubling/adding method [*Lacis and Hansen*, 1974] with single Gauss point adaptation to reproduce the solar zenith angle dependence for reflected solar radiation by clouds and aerosols with the same degree of precision as the full doubling-adding for conservative scattering. The six spectral intervals are superimposed with twelve absorption coefficient profiles to account for overlapping absorption.

2.1. Online Aerosol Simulation

[9] Anthropogenic emissions include the seasonal emissions of SO_2 from fossil fuel combustion, industrial activities [*Baughcum et al.*, 1993; *Benkovitz et al.*, 1996] and biomass burning [*Spiro et al.*, 1992] compiled by the Global Emission Inventory Activity (GEIA) [*Guenther et al.*, 1995]. Natural emissions include SO_2 from noneruptive volcanoes [*Spiro et al.*, 1992] and oceanic DMS [*Liss and Merlivat*, 1986; *Kettle et al.*, 1999]. Anthropogenic and natural emissions of NH_3 from domestic animals, fertilizers, soils and crops, oceans, biomass burning and humans are also considered [*Bouwman et al.*, 1997].

[10] Global aerosol mass concentrations are simulated online [*Adams et al.*, 1999, 2001; *Koch et al.*, 1999]. Aerosol is internally mixed, composed of sulfate (SO_4^{2-}), ammonium (NH_4^+), nitrate (NO_3^-), methanesulfonic acid (MSA) and water. Gas phase species simulated are dimethyl sulfide (DMS), sulfur dioxide (SO_2), ammonia (NH_3) and hydrogen peroxide (H_2O_2). Gas phase reactions considered are of DMS with hydroxyl (OH) and nitrate (NO_3) radicals and oxidation of SO_2 by OH. In-cloud formation of SO_4^{2-} from the oxidation of HSO_3^- by H_2O_2 is also considered. Volatile inorganic species (NH_4^+, NO_3^-, H_2O) are assumed to be in thermodynamic equilibrium over the 1-hour model time step [*Adams et al.*, 1999]; ISORROPIA [*Nenes et al.*, 1998, 1999] determines the partitioning of the volatile chemical species, ammonia, nitrate and water between the gas and the aerosol phase based on the temperature, relative humidity and amount of aerosol precursor in each grid cell.

[11] The aerosol simulation has been extensively evaluated with a wide variety of observations [*Adams et al.*, 1999; *Koch et al.*, 1999]. Simulated concentrations of sulfate and ammonium generally agree within a factor of two with EMEFS and EMEP observations. Annual average nitrate concentrations are not reproduced as well, likely from uncertainties in measurements in aerosol nitrate [*Yu et al.*, 2005], to uncertainty in predicted ammonium and sulfate (which control aerosol pH, hence nitrate partitioning) and interaction of HNO_3 with dust and sea salt.

2.2. Aerosol-Cloud Interactions

[12] Aerosol microphysical parameters for CDNC calculations are obtained by scaling prescribed aerosol size distributions to the simulated online sulfate mass concentration (section 2.1); aerosol nitrate is subject to considerable error and therefore is not considered. Two types of aerosol size distributions are prescribed: (1) marine, for grid cells over the ocean, and, (2) continental, for grid cells over land (Table 1). Both aerosol types are assumed to be a mixture of ammonium sulfate and insoluble material.

[13] CDNC is computed using the physically based parameterization of *Fountoukis and Nenes* [2005]. This

Table 1. Trimodal Lognormal Aerosol Size Distributions Used in This Study[a]

	Nuclei Mode				Accumulation Mode				Coarse Mode			
Aerosol Type	D_g	σ	N_{ap}	χ_{SO4}	D_g	σ	N_{ap}	χ_{SO4}	D_g	σ	N_{ap}	χ_{SO4}
Marine	0.020	1.47	230	0.33	0.092	1.60	177	0.33	0.580	2.49	3.10	0.95
Continental	0.016	1.60	1000	0.50	0.067	2.10	800	0.50	0.930	2.20	0.72	0.50

[a] D_g is the modal geometric mean diameter (μm), N_{ap} is the mode concentration (cm^{-3}), σ is the geometric standard deviation, and χ_{SO4} is the sulfate mass fraction. Distributions obtained from *Whitby* [1978].

parameterization is one of the most comprehensive and computationally efficient formulations available for global models. Its accuracy has been evaluated with detailed numerical simulations [*Nenes and Seinfeld*, 2003; *Fountoukis and Nenes*, 2005] and in situ data for cumuliform and stratiform clouds of marine and continental origin [*Meskhidze et al.*, 2005; *Fountoukis et al.*, 2007]. The parameterization is based on the framework of an ascending cloud parcel; the maximum supersaturation, s_{max}, controls CDNC and is determined by the balance of water vapor availability from cooling and depletion from the condensational growth of activated droplets. The concept of ''population splitting'' (in which droplets are classified by the proximity to their critical diameter) allows s_{max} to be determined from the numerical solution of an algebraic equation. Population splitting also allows the accurate treatment of complex aerosol chemistry and kinetic limitations on droplet growth, such as from the presence of organics that depress surface tension and water vapor uptake [e.g., *Fountoukis and Nenes*, 2005].

[14] In our simulations, a single cloud-base updraft velocity is prescribed to compute droplet number, which for the ''base case'' simulation is set to 1 m s^{-1} over land and 0.5 m s^{-1} over ocean. The ''base case'' value of water vapor mass uptake coefficient, α_c, is set to 0.042, consistent with laboratory [*Pruppacher and Klett*, 1997; *Shaw and Lamb*, 1999], and in situ CDNC closure studies [*Conant et al.*, 2004; *Meskhidze et al.*, 2005; *Fountoukis et al.*, 2007]. The sensitivity of our simulations to the updraft velocity and α_c is also considered (section 6).

3. Quantification of CCN Prediction Error

[15] In situ measurements of aerosol size distribution, chemical composition and CCN concentrations are used for characterizing CCN prediction error. The data was obtained at the Atmospheric Investigation, Regional Modeling, Analysis and Prediction (AIRMAP) Thompson Farm (TF) site (Durham, NH) during the ICARTT (International Consortium for Atmospheric Research on Transport and Transformation) campaign (July–August 2004). TF aerosol is primarily regional, influenced by some local biogenic emissions from the surrounding forest [e.g., *DeBell et al.*, 2004].

[16] CCN concentrations were measured at 0.20, 0.30, 0.37, 0.50, and 0.60% s, with a Droplet Measurement Technologies, Inc. (DMT) streamwise thermal gradient cloud condensation nuclei counter [*Roberts and Nenes*, 2005; *Lance et al.*, 2006]. Throughout the measurement period, the CCN counter operated at a flow rate of 0.5 L min^{-1} with a sheath-to-aerosol flow ratio of 10:1. CCN concentrations were measured at each s for 6 minutes yielding a spectrum every 30 minutes. Measurements of the aerosol size distribution were obtained every two minutes for mobility diameters between 7 and 289 nm with a TSI Scanning Mobility Particle Sizer (SMPS, model 3080, which included a TSI model 3010 Condensation Particle Counter (CPC) and a TSI model 3081L long Differential Mobility Analyzer (DMA)). Simultaneously, size-resolved chemical composition was measured every 10 minutes with an Aerodyne Aerosol Mass Spectrometer (AMS) [*Jayne et al.*, 2000].

[17] For most of the period, polluted continental air was sampled from the Great Lakes; roughly equal amounts of freshly condensed secondary organic aerosols (SOA) and primary organic carbon (POA) composed the carbonaceous fraction (L. D. Cottrell et al., Submicron particles at Thompson Farm during ICARTT measured using aerosol mass spectrometry, manuscript in preparation, 2007, hereinafter referred to as Cottrell et al., manuscript in preparation, 2007). Occasionally, polluted rural air (characterized by higher CCN concentrations and larger sulfate mass fractions) was collected from south of the sampling site. The sulfate mass fraction ranged in our data set between 0.06 and 0.54, with an average of 0.24 ± 0.09. Sulfate and ammonium always dominated the inorganic fraction. The aerosol number concentration ranged between 1366 and 8419 cm^{-3} with an average of 3786 ± 1360 cm^{-3}. A detailed description and analysis of the data set is given by *Medina et al.* [2007] and Cottrell et al. (manuscript in preparation, 2007).

[18] Köhler theory, combined with the observed aerosol size distribution and chemical composition from the ICARTT campaign yields ''predicted'' CCN concentrations. Following *Sotiropoulou et al.* [2006], both ''predicted'' and ''observed'' CCN concentrations are fit to the ''modified power law'' form of *Cohard et al.* [1998, 2000], where CCN approach a constant value at high supersaturations (which in this study is taken to be the total aerosol number). The ''modified power law'' is selected for its simplicity, and ability to describe a CCN spectrum for a very wide range of supersaturations [*Cohard et al.*, 1998, 2000].

[19] The degree of CCN closure is typical of polluted environments and larger than for pristine ones [*Medina et al.*, 2007, and references therein]; using size-averaged chemical composition, CCN closure is achieved within 36 ± 29%, while introducing size-dependent chemical composition CCN concentrations is overpredicted by 17 ± 27%. Under certain conditions (e.g., externally mixed aerosol or freshly emitted carbonaceous aerosol) the closure error may be larger; whether or not this is important enough to have a global impact remains to be seen. For this study,

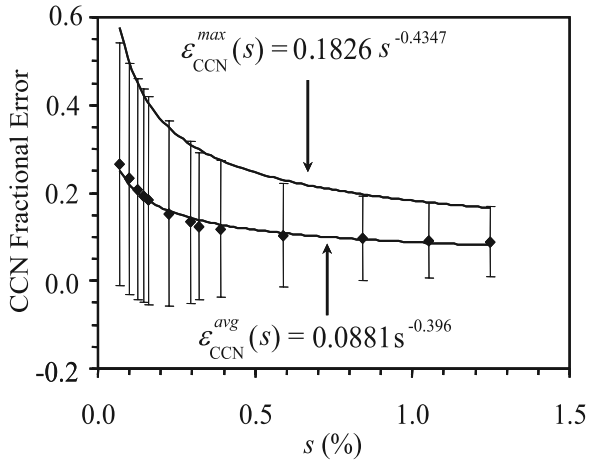

Figure 1. Average and maximum fractional CCN prediction error obtained from the ICARTT data set [*Medina et al.*, 2007].

we will assume that the TF data set can be used to estimate the CCN prediction error throughout the globe.

[20] The CCN prediction error, $\varepsilon_{CCN}(s)$, is then expressed in fractional form as,

$$\varepsilon_{CCN}(s) = \frac{F_o(s) - F_p(s)}{F_o(s)} \tag{2}$$

where $F(s)$ is the CCN concentration as a function of s (i.e., the CCN "spectrum"), subscript "o" refers to observations, and "p" to predictions. From the CCN spectra of the data set, we compute the average fractional error, $\varepsilon_{CCN}^{avg}(s)$, and its standard deviation, $\sigma_{CCN}(s)$. Using least squares minimization, $\varepsilon_{CCN}^{avg}(s)$ and the maximum fractional error, $\varepsilon_{CCN}^{max}(s) = \varepsilon_{CCN}^{avg}(s) + \sigma_{CCN}(s)$, can be expressed as (Figure 1),

$$\begin{aligned} \varepsilon_{CCN}^{avg}(s) &= 0.0881 s^{-0.3960} \\ \varepsilon_{CCN}^{max}(s) &= 0.1826 s^{-0.4347} \end{aligned} \tag{3}$$

$\varepsilon_{CCN}^{avg}(s)$ corresponds to the average CCN prediction error when considering size-resolved aerosol composition (i.e., computing CCN using the measurements of size-dependent composition); $\varepsilon_{CCN}^{max}(s)$ corresponds to the average CCN prediction error when the aerosol is assumed to have a size-invariant composition (i.e., the size-averaged composition is used in the calculation of CCN concentrations [*Medina et al.*, 2007]).

4. Implications for CDNC, Indirect Forcing, and Autoconversion Rate

[21] The "base case" model simulation corresponds to present day emissions (year 2000), from which the "base case" s_{max}, CDNC, shortwave (SW) cloud forcing at the top of the atmosphere (TOA) and autoconversion rate are determined. In each grid cell and model time step, $\varepsilon_{CCN}^{avg}(s)$ and $\varepsilon_{CCN}^{max}(s)$ are computed using equation (3) and the "base case" s_{max}. The "base case" size distribution, F^{base}, is then varied so that the change in CCN at s_{max} corresponds to $\varepsilon_{CCN}^{avg}(s)$ and $\varepsilon_{CCN}^{max}(s)$ as,

$$\begin{aligned} F^{avg^+} &= \left[1 + 0.5\varepsilon_{CCN}^{avg}(s_{max})\right] F^{base} \\ F^{avg^-} &= \left[1 - 0.5\varepsilon_{CCN}^{avg}(s_{max})\right] F^{base} \\ F^{max^+} &= \left[1 + 0.5\varepsilon_{CCN}^{max}(s_{max})\right] F^{base} \\ F^{max^-} &= \left[1 - 0.5\varepsilon_{CCN}^{max}(s_{max})\right] F^{base} \end{aligned} \tag{4}$$

where $F^{avg^+}(F^{avg^-})$ is F^{base} scaled to the upper (lower) limit of average error $\varepsilon_{CCN}^{avg}(s_{max})$, and, F^{max^+} (F^{max^-}) is F^{base} scaled to the upper (lower) limit of maximum error $\varepsilon_{CCN}^{max}(s_{max})$. In applying equation (4) we have assumed that $\varepsilon_{CCN}^{avg}(s_{max}) = \frac{F^{avg^+} - F^{avg^-}}{F^{base}}$ and $\varepsilon_{CCN}^{max}(s_{max}) = \frac{F^{avg^+} - F^{avg^-}}{F^{base}}$.

[22] The modified distributions in equation (4) are introduced into the activation parameterization to compute its importance for predictions of CDNC, first aerosol indirect forcing and autoconversion rate. Figure 2 outlines the calculation procedure.

4.1. CDNC Error

[23] The average, ε_{CDNC}^{avg}, and maximum, ε_{CDNC}^{max}, fractional CDNC error are calculated as,

$$\begin{aligned} \varepsilon_{CDNC}^{avg} &= \left| \frac{N_d^{avg^+} - N_d^{avg^-}}{N_d^{base}} \right| \\ \varepsilon_{CDNC}^{max} &= \left| \frac{N_d^{max^+} - N_d^{max^-}}{N_d^{base}} \right| \end{aligned} \tag{5}$$

where N_d^{base} is the CDNC for the "base case" scenario, and $N_d^{avg^+}$, $N_d^{avg^-}$, $N_d^{max^+}$ and $N_d^{max^-}$ are the CDNC corresponding to F^{avg^+}, F^{avg^-}, F^{max^+} and F^{max^-}, respectively (Figure 2). Normalization in each grid cell is done by using monthly mean droplet number concentrations.

4.2. Indirect Forcing Error

[24] Calculation of the SW TOA cloud forcing is done using the GCM radiative transfer routine. The cloud optical depth in each GCM grid cell is calculated as,

$$\tau = \left(\frac{9\pi\kappa P^3 h^3 q_l^2 N_d}{2\rho_w^2 g^3 C_l^2 \rho} \right)^{\frac{1}{3}} \tag{6}$$

where τ is the cloud optical depth, h is the thickness of the sigma layer, P is the pressure (N m^{-2}), q_l is the grid-averaged liquid water mixing ratio, N_d is the cloud droplet number concentration (m^{-3}) calculated by the *Fountoukis and Nenes* [2005] parameterization, ρ_w is the density of water (kg m^{-3}), ρ is the density of air (kg m^{-3}), g is the gravitational acceleration (m s^{-2}), C_l is the grid cell cloud fraction. κ relates the volumetric radius to effective radius, and is assumed to be 0.67 for continental air masses and 0.80 for maritime air masses [*Martin et al.*, 1994].

[25] GCM vertical resolution is too coarse to resolve clouds and optical thickness is overestimated by assuming the grid box is vertically full with cloud. This issue is addressed by introducing a corrected optical depth, τ', in the radiative calculation [*Del Genio et al.*, 1996],

$$\tau' = \tau C_l^{1/3} \tag{7}$$

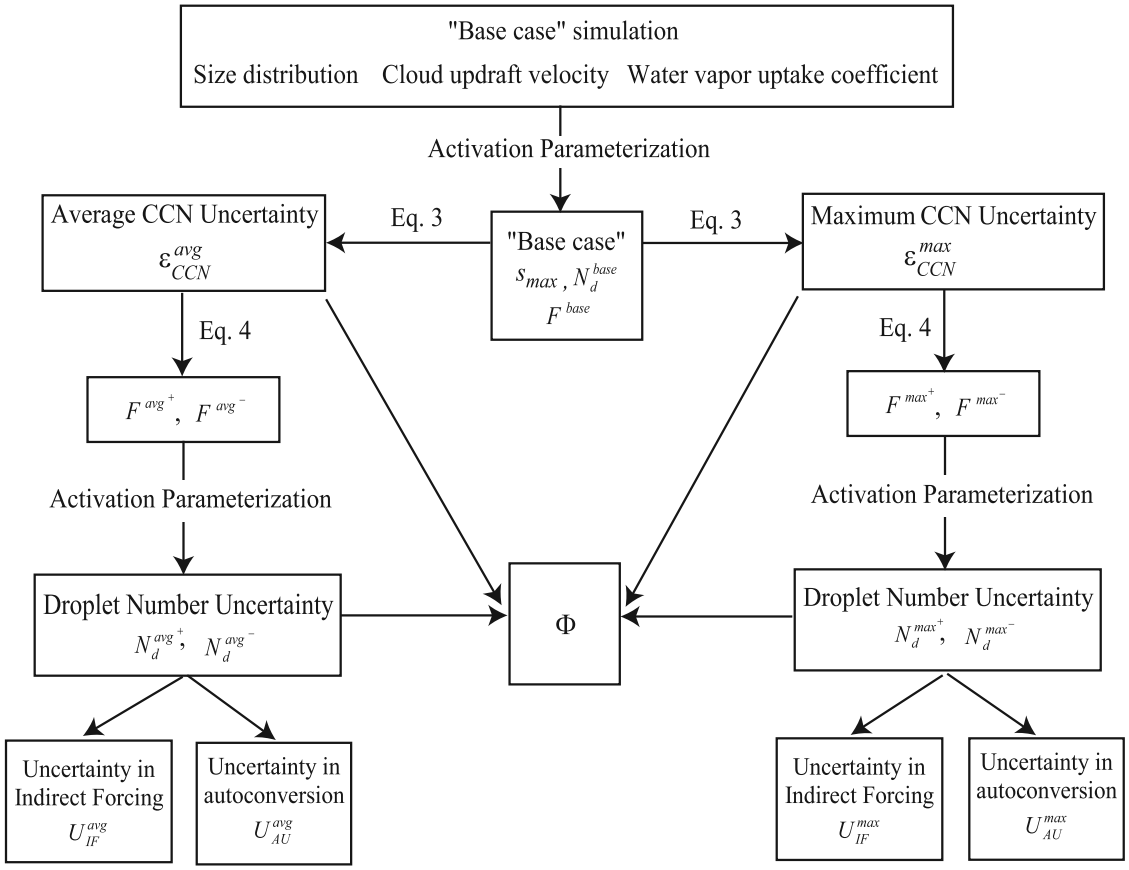

Figure 2. Methodology used for estimating the error in CCN, CDNC, indirect forcing and autoconversion rate.

[26] The average, U_{IF}^{avg}, and maximum, U_{IF}^{max}, error in indirect forcing arising from CCN prediction error is,

$$U_{IF}^{avg} = \left| CF_{TOA}^{avg^+} - CF_{TOA}^{avg^-} \right| \qquad U_{IF}^{max} = \left| CF_{TOA}^{max^+} - CF_{TOA}^{max^-} \right| \tag{8}$$

where $CF_{TOA}^{avg^+}$, $CF_{TOA}^{avg^-}$, $CF_{TOA}^{max^+}$, and $CF_{TOA}^{max^-}$ are the SW TOA cloud forcings for optical depths corresponding to F^{avg^+}, F^{avg^-}, F^{max^+} and F^{max^-}, respectively.

4.3. Impact on Autoconversion Rate

[27] Results are expressed in terms of the average, U_{AU}^{avg}, and maximum, U_{AU}^{max}, fractional error in autoconversion rate,

$$U_{AU}^{avg} = \left| \frac{(\dot{q}_l)_{AU}^{avg^+} - (\dot{q}_l)_{AU}^{avg^-}}{(\dot{q}_l)_{AU}^{base}} \right| \qquad U_{AU}^{max} = \left| \frac{(\dot{q}_l)_{AU}^{max^+} - (\dot{q}_l)_{AU}^{max^-}}{(\dot{q}_l)_{AU}^{base}} \right| \tag{9}$$

where $(\dot{q}_l)_{AU}^{base}$ is the "base case" autoconversion rate, $(\dot{q}_l)_{AU}^{avg^+}$, $(\dot{q}_l)_{AU}^{avg^-}$, $(\dot{q}_l)_{AU}^{max^+}$ and $(\dot{q}_l)_{AU}^{max^-}$ are the autoconversions corresponding to F^{avg^+}, F^{avg^-}, F^{max^+} and F^{max^-}, respectively. Normalization in each grid cell is done by using monthly mean autoconversion rates.

[28] Autoconversion rates vary substantially between parameterizations; to assess the robustness of our results, we repeat the error calculation for multiple autoconversion formulations. We use the parameterizations of *Rotstayn* [1997] and *Khairoutdinov and Kogan* [2000], which explicitly consider CDNC. *Rotstayn* [1997] modified the work of *Manton and Cotton* [1977] to account for the fractional cloudiness often encountered in a GCM grid cell,

$$(\dot{q}_l)_{AU} = -C_l \frac{0.104 g E_{AU} \rho^{\frac{4}{3}}}{\mu (N_d \rho_w)^{\frac{1}{3}}} \left(\frac{q_l}{C_l}\right)^{\frac{7}{3}} H\left(\frac{q_l}{C_l} - q_{CR}\right) \tag{10}$$

where μ is the dynamic viscosity of air (kg m^{-1} s^{-1}), and E_{AU} is the mean collection efficiency (assumed to be 0.55). H is the Heaviside function which suppresses autoconversion until $\frac{q_l}{C_l}$ reaches a "critical" liquid water mixing ratio, $q_{CR} = \frac{4}{3}\pi\rho_w r_{CR}^3 N_d/\rho$ (where r_{CR} is the "critical" volume-mean cloud droplet radius for the onset of autoconversion, set to 7.5 μm).

[29] *Khairoutdinov and Kogan* [2000] developed their parameterizations using Large Eddy Simulations of stratocumulus cloud fields. Two formulations are provided, one explicitly in terms of droplet number,

$$(\dot{q}_l)_{AU} = 1350 C_l \left(\frac{q_l}{C_l}\right)^{2.47} \left(N_d \times 10^{-6}\right)^{-1.79} \tag{11}$$

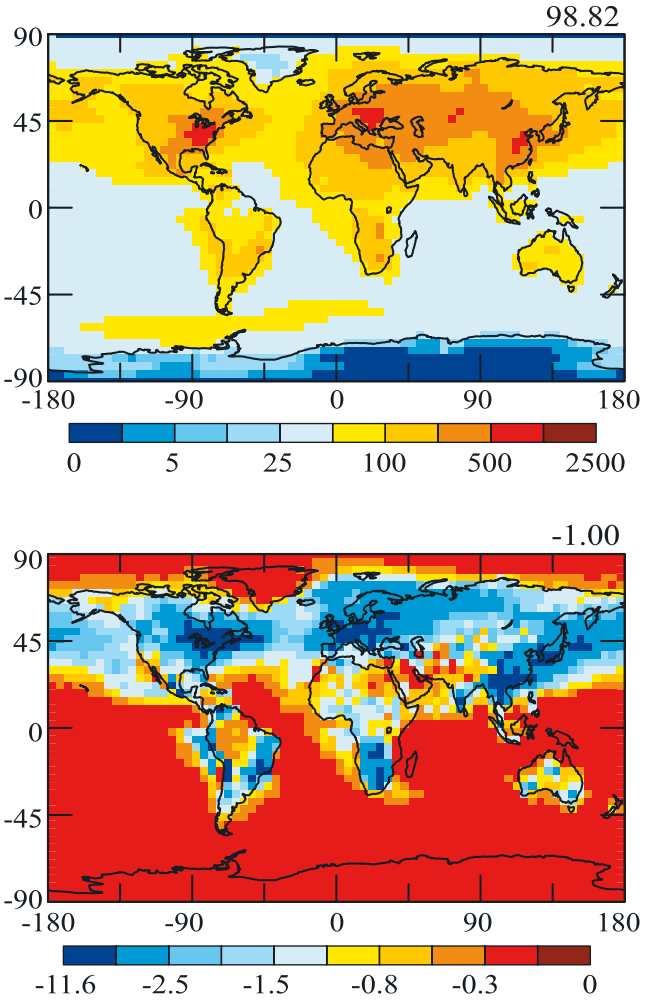

Figure 3. (top) "Base case" annual mean cloud droplet number concentrations (cm^{-3}) and (bottom) anthropogenic aerosol indirect forcing ($W\ m^{-2}$). The global average is shown in the upper right hand corner of each panel.

and another, in terms of drop mean volume radius, r_v (μm):

$$(\dot{q}_l)_{AU} = 4.1 \times 10^{15} C_l r_v^{5.67} \quad (12)$$

Equations (11) and (12) have been modified to account for the fractional cloud cover in the GCM grid cell.

[30] Equations (10), (11), and (12) consider changes in autoconversion from increases in submicron CCN concentrations, but not the impact of giant CCN (GCCN) on drizzle formation. The latter have been shown to accelerate the formation of drizzle in numerous remote sensing [*Rosenfeld et al.*, 2002; *Rudich et al.*, 2002] and modeling studies [*Levin et al.*, 1996; *Reisin et al.*, 1996; *Feingold et al.*, 1999; *Yin et al.*, 2000; *Zhang et al.*, 2006]. Despite their potential importance, including the impact of GCCN on autoconversion is challenging (and currently not considered in parameterizations) because of the highly nonlinear physics involved and the lack of observational constraints. GCCN impacts may not be as important in our study, because we are assessing autoconversion changes that arise from differences in aerosol chemical composition (more exactly, its size dependence), but not size distribution. Shifts in composition would not affect concentrations of GCCN in all of the simulations, as their large size (i.e., very low critical supersaturation) ensures that they would always activate, regardless of their composition. Thus GCCN impacts on cloud microphysics will affect primarily the "base case" value of autoconversion but not its sensitivity to modest changes in CCN concentrations. It should be noted however that our simulations do not completely neglect the presence of GCCN; their impact on s_{max} (by competing for water vapor) is considered, as our prescribed lognormal distributions predict nonnegligible concentrations of GCCN in most regions of the globe.

5. Results and Discussion

5.1. Base Case Simulation

[31] Figure 3 presents the "base case" annual mean CDNC (Figure 3, top) and preindustrial-current day aerosol indirect forcing (Figure 3, bottom). Largest values of CDNC are predicted in the midlatitudes of the Northern Hemisphere, downwind of sources in industrialized regions. High values of CDNC are also seen in the North Atlantic, from long-range transport of pollution plumes, and in the Southern Hemisphere downwind of biomass burning regions. Figure 3 also illustrates the annual mean anthropogenic aerosol indirect forcing (Figure 3, bottom), defined as the difference in the TOA net shortwave incoming flux between the present-day and preindustrial simulations. The globally averaged TOA indirect radiative forcing is $-1.00\ W\ m^{-2}$, consistent with most assessments to date [e.g., *Suzuki et al.*, 2004; *Lohmann and Feichter*, 2005]. The spatial pattern of indirect forcing tends to follow that of CDNC, with largest values ($\sim -10\ W\ m^{-2}$) computed downwind of industrialized regions of the globe.

5.2. Fractional CCN Error

[32] The spatial distributions of ε_{CCN}^{avg} and ε_{CCN}^{max} in the model surface layer are presented in Figure 4. The global average ε_{CCN}^{avg} (Figure 4a) is 0.09 (i.e., 9%), and the global mean ε_{CCN}^{max} (Figure 4b) is 0.18 (i.e., 18%). Larger CCN prediction error is found where in-cloud s_{max} is low, such as in regions affected by industrial pollution plumes (North America, Europe) and long-range transport of pollution plumes (North Atlantic). Between 20 and 60°N, the annual mean ε_{CCN}^{avg} (ε_{CCN}^{max}) is 0.10 (0.21); for the continental United States the corresponding values are 0.10 (0.22), and for Europe, 0.11 (0.24). In pristine areas, in-cloud s_{max} is high (between 1% and 2%), suppressing CCN prediction error (which ranges between 0.09 and 0.15). The above analysis suggests that assuming internally mixed aerosols with a size-invariant chemical composition (expressed by ε_{CCN}^{max}) results in twice the CCN prediction error compared to assuming size-resolved chemical composition (expressed by ε_{CCN}^{avg}). Variations in CCN concentration changes cloud s_{max} 0.04% between F^{avg^+} and F^{avg^-}, and 0.08% between F^{max^+} and F^{max^-}.

5.3. Fractional CDNC Error

[33] Figure 4 presents ε_{CDNC}^{avg} (Figure 4c) and ε_{CDNC}^{max} (Figure 4d) that result from ε_{CCN}^{avg} (Figure 4a) and ε_{CCN}^{max} (Figure 4b), respectively. Since CCN changes generally

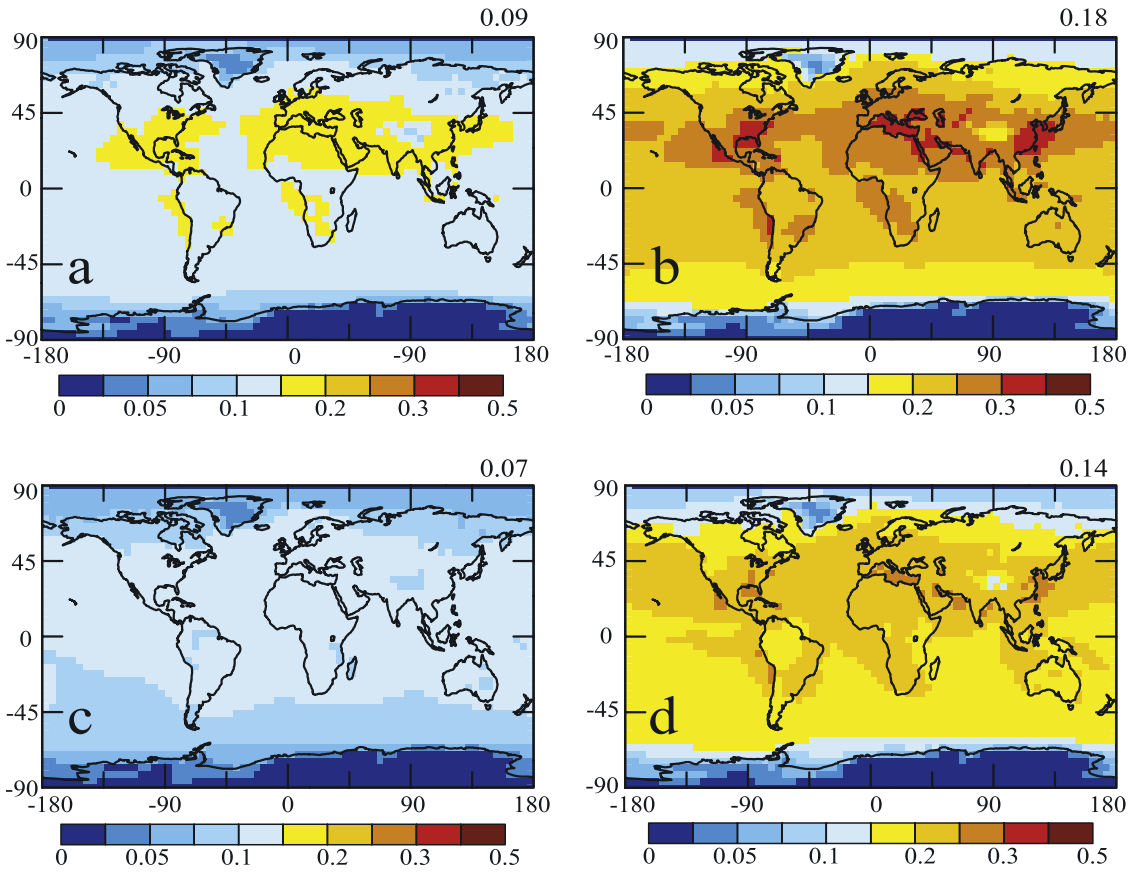

Figure 4. Annual average surface layer (a) ε_{CCN}^{avg}, (b) ε_{CCN}^{max}, (c) ε_{CDNC}^{avg}, and (d) ε_{CDNC}^{max}. The global average value is shown in the upper right hand corner of each panel.

lead to a sublinear response in CDNC, ε_{CDNC} is spatially correlated with ε_{CCN}, but is of smaller magnitude. Larger values of CDNC error are predicted over continents in the Northern Hemisphere; between 20 and 60°N, ε_{CDNC}^{avg} is 0.08 and ε_{CDNC}^{max} is 0.17. The same applies over Europe and the continental US, while CDNC error over pristine regions tends to be smaller, ranging between 0.05 and 0.15 (Figure 4). In summary, CCN prediction error implies a 8–17% CDNC error in polluted regions, and a 5–15% error in pristine regions of the globe.

5.4. Relative Sensitivity of CDNC to CCN

[34] Dividing the fractional errors yields the relative sensitivity of CDNC to CCN error, Φ:

$$\Phi = \frac{\varepsilon_{CCN}^{avg}(s_{max})}{\varepsilon_{CDNC}^{avg}} \quad \text{or} \quad \frac{\varepsilon_{CCN}^{max}(s_{max})}{\varepsilon_{CDNC}^{max}} \tag{13}$$

[35] Low values of Φ suggest high sensitivity of CDNC to CCN prediction error and vice versa.

[36] Figure 5 presents the spatial distribution of the annual Φ. Smaller values of Φ are observed over pristine regions, where CCN and CDNC concentrations are low, hence CDNC are more sensitive to CCN prediction error. The highest Φ is predicted for polluted regions, such as SW USA, Europe, and Asia. In such regions, the large error in predicted CCN concentrations does not translate to large error in CDNC, because dynamical readjustment of in-cloud s_{max} under polluted conditions tends to compensate for changes in CCN. The area NE of India (Tibetan plateau) has a Φ value close to unity, because CCN concentrations are low and in-cloud s_{max} is high. The annual average Φ between 20 and 60°N is 1.22; for USA and Europe, Φ ranges between 1.25 and 1.30. This means that CDNC error is 22–30% lower than CCN prediction error for polluted regions of the globe.

5.5. Impact of CCN Error on Cloud Radiative Forcing

[37] The spatial distributions of U_{IF}^{avg}, and U_{IF}^{max} are shown in Figures 6a and 6b, respectively. The average error

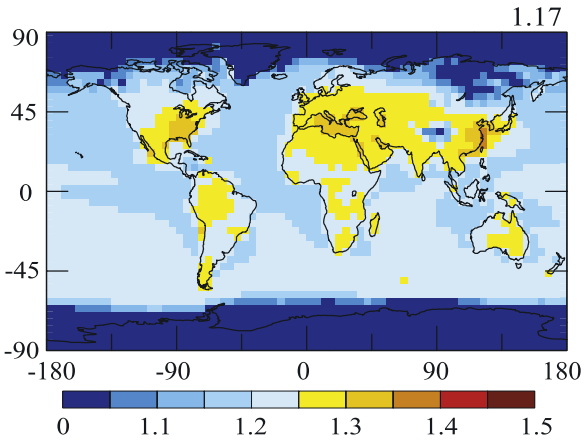

Figure 5. Annual mean Φ in the model surface layer. The global average is shown in the upper right hand corner.

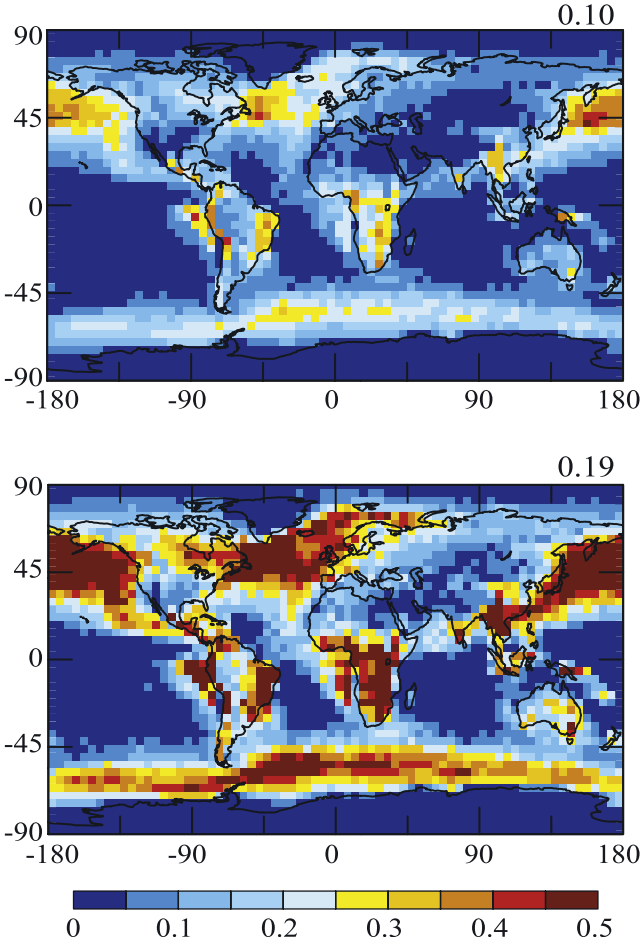

Figure 6. Annual average (top) U_{IF}^{avg} and (bottom) U_{IF}^{max}, expressed in W m^{-2}. The global average value is shown in the upper right hand corner of each panel.

in indirect forcing is equal to 0.1 W m^{-2} while the corresponding maximum error is equal to 0.2 W m^{-2}. Thus CCN prediction error leads to a 10–20% error in global indirect effect. Regionally, indirect forcing error is highest (~0.5 W m^{-2}) downwind of industrialized and biomass burning regions; SW forcing in the surface layer of the oceans is thus subject to a 5–20% error. The least indirect forcing error is predicted over deserts and the subtropical southern oceans, where anthropogenic CCN perturbations are least effective in affecting cloud optical depth.

5.6. Impact of CCN Error on Autoconversion Rate

[38] Autoconversion parameterizations are usually "tuned" to reproduce observations; we did not follow this procedure to explore the robustness of U_{AU}^{avg} and U_{AU}^{max}, in the absence of tuning. Figure 7 presents "base case" autoconversion rates for each parameterization considered in this study (equations (1) and (10)–(12)). All parameterizations are anticorrelated with the spatial patterns of CDNC (Figure 3), but differ substantially (a factor of 20) in predicted autoconversion rate. Compared to the "default" GISS autoconversion scheme (equation (1)), *Khairoutdinov and Kogan* [2000] predicts lower autoconversion and *Rotstayn*'s [1997], higher (Figure 7). The difference between the parameterizations are not a result of error in predicted cloud microphysical characteristics (droplet number concentration, liquid water content), but rather an inherent error in the parameterizations. Compared to the parameterization of *Rotstayn* [1997], the contrast between land and sea is larger using *Khairoutdinov and Kogan*'s [2000] parameterization; this is not surprising, given the stronger dependence of equation (11) on CDNC. The discrepancy between formulations could be reduced if the parameterizations are tuned to match observations; this is beyond the scope of this study.

[39] The average and maximum errors in autoconversion rates using the schemes of *Khairoutdinov and Kogan* [2000] and *Rotstayn* [1997] are shown in Figure 8. The largest autoconversion error is predicted for polluted regions, because pristine clouds, contrary to their polluted counterparts, have a high precipitation efficiency (since their droplets are generally large) hence are less sensitive to CDNC error. The autoconversion schemes of *Khairoutdinov and Kogan* [2000] are most sensitive to N_d, hence CDNC error (Table 2). As a result, the percent U_{AU}^{avg} (U_{AU}^{max}) induced by Köhler theory using equation (11) is 5.6% (11.4%), while the corresponding one using equation (10) is 2.3% (4.7%).

6. Sensitivity Tests

[40] It is instructive to explore the sensitivity of our findings to poorly constrained parameters that influence cloud droplet formation, namely, updraft velocity and α_c. The sensitivity tests are done for conditions that would decrease in-cloud s_{max}; simulations for higher s_{max} are not required, as that would further decrease the already small "base case" error in CDNC and indirect forcing.

[41] It is well known that droplet number is a strong function of updraft velocity, as it controls the parcel expansion rate (i.e., cooling rate), hence parcel supersaturation, droplet concentration, size and the time available for coalescence. At cloud base, a decrease in updraft velocity decreases CDNC and vice versa (everything else being equal). Since cloud-base updrafts are not explicitly resolved in GCMs, but prescribed (as is done in this study) or diagnosed from turbulent kinetic energy, it constitutes a major source of error in CDNC calculations. We repeat the "base case" simulation, but for updraft velocity equal to 0.5 m s^{-1} over land and 0.25 m s^{-1} over ocean.

[42] α_c, formally defined as the probability of a water vapor molecule remaining in the liquid phase upon collision with a droplet [*Seinfeld and Pandis*, 1998], is a parameter which determines the size dependence of the water vapor mass transfer coefficient. Despite the considerable work to date [see *Fountoukis and Nenes*, 2005, and references therein], α_c is still subject to substantial error [e.g., *Fountoukis et al.*, 2007], partly because it is used to parameterize the effect of multiple kinetic limitations, not only accommodation of water molecules in the gas-liquid interface. To account for this error, we repeat the "base case" simulation for $\alpha_c = 1$, which decreases global s_{max} since droplet growth is accelerated in the initial stages of cloud formation.

6.1. Sensitivity to Updraft Velocity

[43] The decrease in updraft velocity leads to a decrease in global s_{max}, from 1.21% in the "base case" simulation to

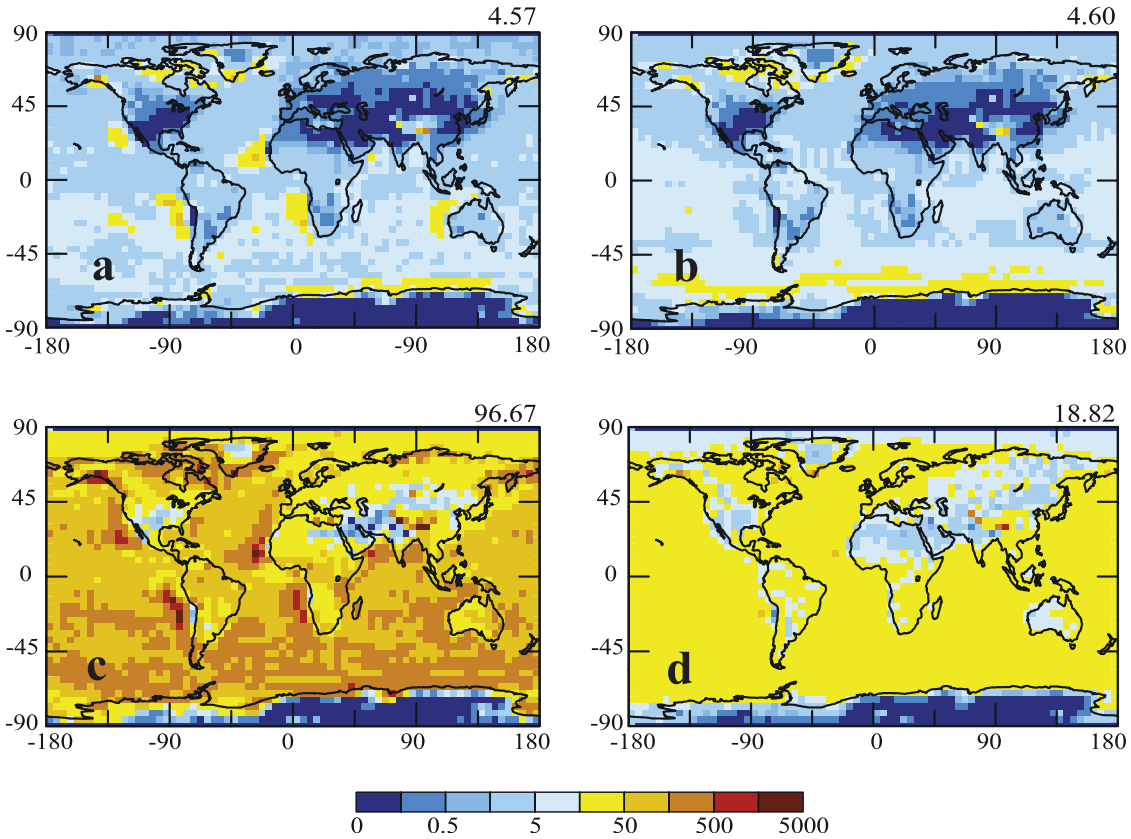

Figure 7. Base case autoconversion rates ($\times 10^{10}$ kg kg^{-1} s^{-1}) as estimated using the autoconversion scheme of (a) *Khairoutdinov and Kogan* [2000] (equation (11)), (b) *Khairoutdinov and Kogan* [2000] (equation (12)), (c) *Rotstayn* [1997] (equation (10)), and (d) equation (1). The global annual average value is shown in the upper right hand corner of each panel.

0.79%. The decrease in s_{max}, however, causes only a slight increase in ε_{CCN}; ε_{CCN}^{avg} is raised from 0.09 to 0.10 globally, from 0.10 to 0.11 between 20–60°N, from 0.10 to 0.12 for USA, and from 0.11 to 0.12 for Europe (Table 2). CDNC error is virtually unaffected; as a result, Φ slightly increases, i.e., CDNC become less sensitive to CCN prediction error (Table 2). U_{IF}^{avg} and U_{AU}^{avg} are also not affected by changes in updraft velocity.

6.2. Sensitivity to Droplet Growth Kinetics

[44] Simulations for $\alpha_c = 1$ decreases global s_{max}, from 1.21% ("base case" simulation) to 0.77%. This leads to a slight increase in ε_{CCN}, with negligible effect on ε_{CDNC}. Specifically, the global ε_{CCN}^{avg} increases to 0.10, while for the region between 20 and 60°N is 0.11 and for the continental US and Europe ε_{CCN}^{avg} is 0.12. Consequently, Φ slightly increases; for the region between 20 and 60°N the annual mean Φ is 1.28; for the continental US the corresponding value is 1.30, while for Europe 1.35. U_{IF}^{avg} and U_{AU}^{avg} are practically unaffected by the change in α_c (Table 2).

7. Implications and Conclusions

[45] The focus of this study is to quantify the error in aerosol indirect radiative forcing and autoconversion rate arising from application of Köhler theory. The GISS GCM Model II' with online aerosol mass simulation and explicit aerosol-cloud coupling is used to quantify the error in indirect forcing and autoconversion rate; CCN prediction error is obtained from a comprehensive data set of aerosol and cloud condensation nuclei (CCN) observations obtained during the ICARTT 2004 campaign. Simulations suggest that the global average CCN prediction error ranges between 10 and 20%; CDNC error ranges between 7 and 14%. Assuming that aerosol is internally mixed and with a size-dependent soluble fraction decreases CCN prediction error twofold, compared to assuming size-invariant chemical composition. These results are insensitive to the range of updraft velocity and water vapor uptake coefficient, and fairly insensitive to the autoconversion parameterization considered.

[46] In terms of indirect forcing, application of Köhler theory introduces a 10–20% error in indirect forcing, both globally and regionally. The regional indirect forcing error can be as high as -0.5 W m^{-2}, but is always a small fraction of the total indirect forcing. This implies that CCN prediction error is not a significant source of error for assessments of the aerosol indirect effect.

[47] Application of Köhler theory does not introduce significant error on global autoconversion (2–11%, depending on the parameterization used). However, for regions affected by pollution and biomass burning, the error can be large, as high as 50%. This implies a large error in

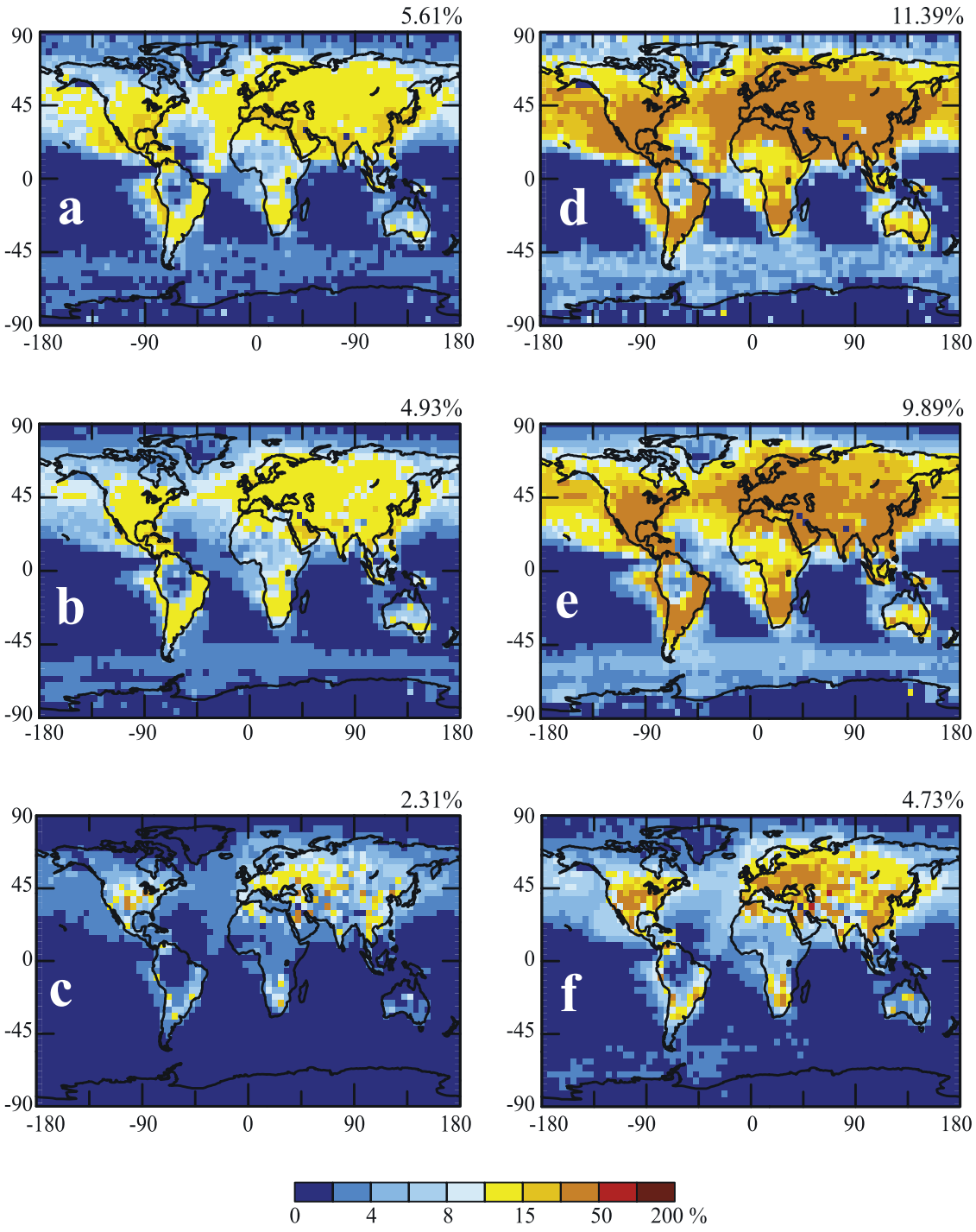

Figure 8. (a–c) Average and (d–f) maximum fractional error in autoconversion rate using the autoconversion parameterizations of *Khairoutdinov and Kogan* [2000], equation (11) (Figures 8a and 8d); *Khairoutdinov and Kogan* [2000], equation (12) (Figures 8b and 8e); and *Rotstayn* [1997], equation (10) (Figures 8c and 8f). The global annual average is shown at the upper right hand corner of each panel.

predictive understanding of the hydrological cycle over climatically sensitive regions of the Earth, such as sub-Saharan Africa, the Midwest region of the United States and East Asia.

[48] Future changes in aerosol levels may affect the error in indirect forcing and autoconversion; this largely depends on whether aerosol burdens will increase, as the latter largely controls in-cloud supersaturation (hence CCN prediction error). However, on the basis of *Sotiropoulou et al.* [2006] and this study, it is unlikely that the error in indirect forcing would exceed 50%, because our simulations suggest that indirect forcing error is roughly proportional to CDNC

Table 2. Annual Average ε_{CCN}^{avg}, ε_{CDNC}^{avg}, Φ, U_{IF}^{avg} (W m^{-2}) and U_{AU}^{avg} (%) for the Three Autoconversion Parameterizations Used[a]

	World			20–60°N			USA			Europe		
Parameter	B	w	α_c	B	w	α_c	B	w	α_c	B	w	α_c
ε_{CCN}^{avg}	0.09	0.10	0.10	0.10	0.11	0.11	0.10	0.12	0.12	0.11	0.12	0.12
ε_{CDNC}^{avg}	0.07	0.09	0.09	0.09	0.09	0.09	0.09	0.09	0.09	0.09	0.09	0.09
Φ	1.17	1.18	1.18	1.19	1.28	1.28	1.23	1.30	1.30	1.26	1.35	1.35
U_{IF}^{avg}	0.10	0.10	0.10	0.14	0.15	0.15	0.10	0.11	0.12	0.09	0.11	0.12
U_{AU}^{avg} (equation (10))	2.31	2.18	2.14	5.22	5.15	5.01	6.93	6.62	6.39	7.48	7.38	7.42
U_{AU}^{avg} (equation (11))	5.61	5.51	5.54	11.23	11.55	11.61	12.76	13.32	13.36	14.38	15.04	15.09
U_{AU}^{avg} (equation (12))	4.93	4.86	4.90	9.50	9.87	9.96	10.95	11.65	11.71	12.09	13.01	13.17

[a]Results are given for (1) "base case" simulation ("B"), (2) "base case" with updraft velocity equal to 0.5 m s^{-1} over land and 0.25 m s^{-1} over ocean ("w"), and (3) "base case" with $\alpha_c = 1$ ("α_c").

error (which for the climatically relevant range of s_{max} is less than 50%). The error however in autoconversion is expected to increase considerably in a more polluted future.

[49] Perhaps the most important implication from this study is on the feasibility of improving indirect forcing assessments. As suggested by the simulations, CCN prediction error may not be an important source of error for indirect forcing, because clouds mostly contributing to the "first" indirect effect are those with moderate levels of pollution (hence higher levels of supersaturation). This means that indirect forcing assessments are not limited by the simplified description of CCN and CDNC formation embodied in state-of-the-art mechanistic parameterizations, and that the error in indirect forcing will decrease as the representation of aerosol, subgrid cloud formation and dynamics are improved in climate models. The same cannot be said about aerosol effects on the hydrological cycle; the precipitation efficiency of clouds is most affected under polluted conditions, where CCN prediction error is largest. This implies that the inherent error in autoconversion and precipitation rate will continue to be large, even as the representation of subgrid cloud processes improve. For the regions subject to the largest error, information on the CCN mixing state may be required to reduce CCN prediction error to less than 10%.

[50] The conclusions of this study are important and require additional work to assess their robustness. First, the CCN closure data set used for estimating the CCN prediction error needs to be expanded to include a wide range of aerosol conditions. Of particular importance are data sets characterizing oceanic regions (both pristine and polluted), biomass-burning aerosol and regions with active chemical ageing, such as pollution mixing with mineral dust. The error assessment should also be repeated with other GCMs, and aerosol-cloud interaction parameterizations to assess the robustness of our conclusions. The CCN prediction error calculation should also be repeated with an aerosol simulation that includes the impact of sea salt, organic and black carbon and mineral dust; inclusion of such species could potentially result in a larger error. The use of a GCM coupled with explicit aerosol microphysics, size-resolved composition and aerosol-cloud interactions [e.g., *Adams and Seinfeld*, 2002] will be the focus of a future study.

[51] **Acknowledgments.** We would like to acknowledge the support from a NASA EOS-IDS, an NSF CAREER award, and a Blanchard-Milliken Young Faculty Fellowship. We would also like to thank L. Oreopoulos for his thoughtful comments.

References

Abdul-Razzak, H., and S. J. Ghan (2000), A parameterization of aerosol activation: 2. Multiple aerosol types, *J. Geophys. Res.*, *105*, 6837–6844.

Abdul-Razzak, H., S. Ghan, and C. Rivera-Carpio (1998), A parameterization of aerosol activation: 1. Single aerosol type, *J. Geophys. Res.*, *103*, 6123–6132.

Adams, P. J., and J. H. Seinfeld (2002), Predicting global aerosol size distributions in general circulation models, *J. Geophys. Res.*, *107*(D19), 4370, doi:10.1029/2001JD001010.

Adams, P. J., J. H. Seinfeld, and D. M. Koch (1999), Global concentrations of tropospheric sulfate, nitrate, and ammonium aerosol simulated in a general circulation model, *J. Geophys. Res.*, *104*, 13,791–13,823.

Adams, P. J., J. H. Seinfeld, D. Koch, L. Mickley, and D. Jacob (2001), General circulation model assessment of direct radiative forcing by the sulfate-nitrate-ammonium-water inorganic aerosol system, *J. Geophys. Res.*, *106*, 1097–1111.

Asa-Awuku, A., and A. Nenes (2007), Effect of solute dissolution kinetics on cloud droplet formation: Extended Khler theory, *J. Geophys. Res.*, doi:10.1029/2005JD006934, in press.

Baughcum, S. L., D. M. Chan, S. M. Happenny, S. C. Henderson, P. S. Hertel, T. Higman, D. R. Maggiora, and C. A. Oncina (1993), Emission scenarios development: Scheduled 1990 and project 2015 subsonic, Mach 2.0 and Mach 2.4 aircraft, in *The Atmospheric Effects of Stratospheric Aircraft: A Third Program Report*, *NASA Ref. Publ.*, *1313*, 89–131.

Benkovitz, C. M., M. T. Scholtz, J. Pacyna, L. Tarrason, J. Dignon, E. C. Voldner, P. A. Spiro, J. A. Logan, and T. E. Graedel (1996), Global gridded inventories of anthropogenic emissions of sulfur and nitrogen, *J. Geophys. Res.*, *101*, 29,239–29,253.

Bouwman, A. F., D. S. Lee, W. A. H. Asman, F. J. Dentener, K. W. Van Der Hoek, and J. G. J. Olivier (1997), A global high-resolution emissions inventory for ammonia, *Global Biogeochem. Cycles*, *11*, 561–587.

Cohard, J.-M., J.-P. Pinty, and C. Bedos (1998), Extending Twomey's analytical estimate of nucleated cloud droplet concentrations from CCN spectra, *J. Atmos. Sci.*, *55*, 3348–3357.

Cohard, J.-M., J.-P. Pinty, and K. Suhre (2000), On the parameterization of activation spectra from cloud condensation nuclei microphysical properties, *J. Geophys. Res.*, *105*, 11,753–11,766.

Conant, W., A. Nenes, and J. H. Seinfeld (2002), Black carbon radiative heating effects on cloud microphysics and implications for the aerosol indirect effect: 1. Extended Köhler theory, *J. Geophys. Res.*, *107*(D21), 4604, doi:10.1029/2002JD002094.

Conant, W. C., et al. (2004), Aerosol-cloud drop concentration closure in warm cumulus, *J. Geophys. Res.*, *109*, D13204, doi:10.1029/2003JD004324.

DeBell, L. J., M. Vozzella, R. W. Talbot, and J. E. Dibb (2004), Asian dust storm events of spring 2001 and associated pollutants observed in New England by the Atmospheric Investigation, Regional, Modeling, Analysis and Prediction (AIRMAP) monitoring network, *J. Geophys. Res.*, *109*, D01304, doi:10.1029/2003JD003733.

Del Genio, A. D., and M.-S. Yao (1993), Efficient cumulus parameterization for long-term climate studies: The GISS scheme, in *The Representation of Cumulus Convection in Numerical Models*, edited by K. A. Emanuel and D. A. Raymond, Meteorol. Monogr., *24* (46), 181–184.

Del Genio, A. D., M.-S. Yao, W. Konari, and K. K.-W. Lo (1996), A prognostic cloud water parameterization for global climate models, *J. Clim.*, *9*, 270–304.

Facchini, M. C., M. Mircea, S. Fuzzi, and R. J. Charlson (1999), Cloud albedo enhancement by surface-active organic solutes in growing droplets, *Nature*, *401*(6750), 257–259.

Feingold, G., W. R. Cotton, S. M. Kreidenweis, and J. T. Davis (1999), The impact of giant cloud condensation nuclei on drizzle formation in stratocumulus: Implications for cloud radiative properties, *J. Geophys. Res.*, *56*, 4100–4117.

Fountoukis, C., and A. Nenes (2005), Continued development of a cloud droplet formation parameterization for global climate models, *J. Geophys. Res.*, *110*, D11212, doi:10.1029/2004JD005591.

Fountoukis, C., et al. (2007), Aerosol-cloud drop concentration closure for clouds sampled during ICARTT, *J. Geophys. Res.*, *112*, D10S30, doi:10.1029/2006JD007272.

Guenther, A., et al. (1995), A global model of natural volatile organic compound emissions, *J. Geophys. Res.*, *100*, 8873–8892.

Hansen, J. E., G. L. Russell, D. Rind, P. Stone, A. Lacis, R. Ruedy, and L. Travis (1983), Efficient three-dimensional models for climatic studies, *Mon. Weather Rev.*, *111*, 609–662.

Intergovernmental Panel on Climate Change (2001), *Climate Change 2001: The Scientific Basis*, Cambridge Univ. Press, Cambridge, U. K.

Jayne, J., D. Leard, X. Zhang, P. Davidovits, K. Smith, C. Kolb, and D. Worsnop (2000), Development of an aerosol mass spectrometer for size and composition analysis of submicron particles, *Aerosol Sci. Technol.*, *33*, 49–70.

Kettle, A. J., et al. (1999), A global database of sea surface dimethylsulfide (DMS) measurements and a procedure to predict sea surface DMS as a function of latitude longitude and month, *Global Biogeochem. Cycles*, *13*, 394–444.

Khairoutdinov, M., and Y. Kogan (2000), A new cloud physics parameterization in a large-eddy simulation model of marine stratocumulus, *Mon. Weather Rev.*, *128*(1), 229–243.

Koch, D., D. Jacob, I. Tegen, D. Rind, and M. Chin (1999), Tropospheric sulfur simulation and sulfate direct radiative forcing in the Goddard Institute for Space Studies general circulation model, *J. Geophys. Res.*, *104*(D19), 23,799–23,822.

Köhler, H. (1921), Zur kondensation des wasserdampfe in der atmosphre, *Geofys. Publ.*, *2*, 3–15.

Kulmala, M., A. Laaksonen, P. Korhonen, T. Vesala, T. Ahonen, and J. Barrett (1993), The effect of atmospheric Nitric-acid vapor on cloud condensation nucleus activation, *J. Geophys. Res.*, *98*(D12), 22,949–22,958.

Lacis, A. A., and J. E. Hansen (1974), A parameterization for the absorption of solar radiation in the Earth's atmosphere, *J. Atmos. Sci.*, *31*, 118–133.

Lance, S., J. Medina, J. N. Smith, and A. Nenes (2006), Mapping the operation of the DMT continuous flow CCN counter, *Aerosol Sci. Technol.*, *40*, 242–254.

Levin, Z., E. Ganor, and V. Gladstein (1996), The effects of desert particles coated with sulfate on rain formation in the eastern Mediterranean, *J. Appl. Meteorol.*, *35*, 1511–1523.

Liss, P. S., and L. Merlivat (1986), Air-sea gas exchange rates: Introduction and synthesis, in *The Role of Air-Sea Exchange in Geochemical Cycling*, pp. 113–127, Reidel, D., Norwell, Mass.

Lohmann, U., and J. Feichter (2005), Global indirect aerosol effects: A review, *Atmos. Chem. Phys.*, *5*, 715–737.

Manton, M. J., and W. R. Cotton (1977), Formulation of approximation equations for modeling moist deep convection on the mesoscale, Atmospheric Science, *Pap. 226*, Dep. of Atmos. Sci., Colo. State Univ., Fort Collins.

Martin, G. M., D. W. Johnson, and A. Spice (1994), The measurement and parameterization of effective radius of droplets in warm stratocumulus clouds, *J. Atmos. Sci.*, *51*, 1823–1842.

Medina, J., A. Nenes, R.-E. P. Sotiropoulou, L. D. Cottrell, L. D. Ziemba, P. J. Beckman, and R. J. Griffin (2007), Cloud condensation nuclei closure during the International Consortium for Atmospheric Research on Transport and Transformation 2004 campaign: Effects of size-resolved composition, *J. Geophys. Res.*, *112*, D10S31, doi:10.1029/2006JD007588.

Meskhidze, N., A. Nenes, W. C. Conant, and J. H. Seinfeld (2005), Evaluation of a new cloud droplet activation parameterization with in situ data from CRYSTAL-FACE and CSTRIPE, *J. Geophys. Res.*, *110*, D16202, doi:10.1029/2004JD005703.

Nenes, A., and J. H. Seinfeld (2003), Parameterization of cloud droplet formation in global climate models, *J. Geophys. Res.*, *108*(D14), 4415, doi:10.1029/2002JD002911.

Nenes, A., C. Pilinis, and S. N. Pandis (1998), ISORROPIA: A new thermodynamic model for inorganic multicomponent atmospheric aerosols, *Aquat. Geochem.*, *4*, 123–152.

Nenes, A., S. N. Pandis, and C. Pilinis (1999), Continued development and testing of a new thermodynamic aerosol module for urban and regional air quality models, *Atmos. Environ.*, *33*, 1553–1560.

Pruppacher, H., and J. Klett (1997), *Microphysics of Clouds and Precipitation*, 2nd ed., Springer, New York.

Reisin, T., S. Tzivion, and Z. Levin (1996), Seeding convective clouds with ice nuclei or hygroscopic particles: A numerical study using a model with detailed microphysics, *J. Appl. Meteorol.*, *35*, 1416–1434.

Roberts, G., and A. Nenes (2005), A continuous-flow streamwise thermal-gradient CCN chamber for atmospheric measurements, *Aerosol Sci. Technol.*, *39*, 206–221, doi:10.1080/027868290913988.

Rosenfeld, D., R. Lahav, A. Khain, and M. Pinsky (2002), The role of sea spray in cleansing air pollution over ocean via cloud processes, *Science*, *297*, 1667–1670, doi:10.1126/science.1073869.

Rotstayn, L. D. (1997), A physically based scheme for the treatment of stratiform clouds and precipitation in large-scale models. 1. Description and evaluation of the microphysical processes, *Q. J. R. Meteorol. Soc.*, *123*, 1227–1282.

Rudich, Y., O. Khersonsky, and D. Rosenfeld (2002), Treating clouds with a grain of salt, *Geophys. Res. Lett.*, *29*(22), 2060, doi:10.1029/2002GL016055.

Seinfeld, J. H., and S. N. Pandis (1998), *Atmospheric Chemistry and Physics: From Air Pollution to Climate Change*, John Wiley, New York.

Shaw, R. A., and D. Lamb (1999), Experimental determination of the thermal accommodation and condensation coefficients of water, *J. Chem. Phys.*, *111*(23), 10,659–10,663.

Shulman, M. L., M. C. Jacobson, R. J. Carlson, R. E. Synovec, and T. E. Young (1996), Dissolution behavior and surface tension effects of organic compounds in nucleating cloud droplets, *Geophys. Res. Lett.*, *23*(3), 277–280.

Sotiropoulou, R. E. P., J. Medina, and A. Nenes (2006), CCN predictions: Is theory sufficient for assessment of the indirect effect?, *Geophys. Res. Lett.*, *33*, L05816, doi:10.1029/2005GL025148.

Spiro, P. A., D. J. Jacob, and J. A. Logan (1992), Global inventory of sulfur emissions with $1° \times 1°$ resolution, *J. Geophys. Res.*, *97*, 6023–6036.

Sundqvist, H., E. Berge, and J. E. Kristjansson (1989), Condenstation and cloud parameterization studies with a mesoscale numerical weather prediction model, *Mon. Weather Rev.*, *117*, 1641–1657.

Suzuki, K., T. Nakajima, A. Numaguti, T. Takemura, K. Kawamoto, and A. Higurashi (2004), A study of the aerosol effect on a cloud field with simultaneous use of GCM modeling and satellite observation, *J. Atmos. Sci.*, *61*, 179–193.

Toon, O. B., and J. B. Pollack (1976), A global average model of atmospheric aerosols for radiaitve transfer calculations, *J. Appl. Meteorol.*, *15*, 225–246.

Whitby, K. T. (1978), Physical characteristics of sulfur aerosols, *Atmos. Environ.*, *12*, 135–159.

Yin, Y., Z. Levin, T. G. Reisin, and S. Tzivion (2000), The effects of giant cloud condensation nuclei on the development of precipitation in convective clouds—A numerical study, *Atmos. Res.*, *53*, 91–116.

Yu, X. Y., L. Taehyoung, B. Ayres, S. M. Kreidenweis, J. L. Collett, and W. Maim (2005), Particulate nitrate measurement using nylon filters, *J. Air Waste Manage. Assoc.*, *55*, 1100–1110.

Zhang, L., D. V. Michelangeli, and P. A. Taylor (2006), Influence of aerosol concentration on precipitation formation in low-level, warm stratiform clouds, *Aerosol Sci.*, *37*, 203–217.

P. J. Adams, Department of Civil and Environmental Engineering, Carnegie Mellon University, Pittsburgh, PA 15213, USA. (petera@andrew.cmu.edu)

A. Nenes and R.-E. P. Sotiropoulou, School of Earth and Atmospheric Sciences, Georgia Institute of Technology, Atlanta, GA 30332, USA. (nenes@eas.gatech.edu; rsot@eas.gatech.edu)

J. H. Seinfeld, Department of Chemical Engineering, California Institute of Technology, Mail Code 210-41, Pasadena, CA 91125, USA. (seinfeld@caltech.edu)